Cross-shell excitations from the fp shell: Lifetime measurements in ^{61}Zn

M. Queiser,[1] A. Vogt,[1,*] M. Seidlitz,[1] P. Reiter,[1] T. Togashi,[2] N. Shimizu,[2] Y. Utsuno,[3,4] T. Otsuka,[5,2,4,6,7] M. Honma,[8] P. Petkov,[1,9] K. Arnswald,[1] R. Altenkirch,[1] B. Birkenbach,[1] A. Blazhev,[1] T. Braunroth,[1] A. Dewald,[1] J. Eberth,[1] C. Fransen,[1] B. Fu,[1] H. Hess,[1] R. Hetzenegger,[1] R. Hirsch,[1] J. Jolie,[1] V. Karayonchev,[1] L. Kaya,[1] L. Lewandowski,[1] C. Müller-Gatermann,[1] J.-M. Régis,[1] D. Rosiak,[1] D. Schneiders,[1] B. Siebeck,[1] T. Steinbach,[1] K. Wolf,[1] and K.-O. Zell[1]

[1]*Institut für Kernphysik, Universität zu Köln, D-50937 Köln, Germany*
[2]*Department of Physics, University of Tokyo, Hongo, Bunkyo-ku, Tokyo 113-0033, Japan*
[3]*Advanced Science Research Center, Japan Atomic Energy Agency, Tokai, Ibaraki 319-1195, Japan*
[4]*Center for Nuclear Study, University of Tokyo, Hongo, Bunkyo-ku, Tokyo 113-0033, Japan*
[5]*RIKEN Nishina Center, 2-1, Hirosawa, Wako, Saitama 351-0198, Japan*
[6]*National Superconducting Cyclotron Laboratory, Michigan State University, East Lansing, Michigan 48824, USA*
[7]*Instituut voor Kern- en Stralingsfysica, KU Leuven, B-3001 Leuven, Belgium*
[8]*Center for Mathematical Sciences, University of Aizu, Ikki-machi, Aizu-Wakamatsu, Fukushima 965-8580, Japan*
[9]*Horia Hulubei National Institute for Physics and Nuclear Engineering, R-76900 Bucharest-Măgurele, Romania*

(Received 5 August 2017; published 10 October 2017)

Lifetimes of excited states in the neutron-deficient nucleus ^{61}Zn were measured employing the recoil-distance Doppler-shift (RDDS) and the electronic fast-timing methods at the University of Cologne. The nucleus of interest was populated as an evaporation residue in ^{40}Ca(^{24}Mg,$n2p$)^{61}Zn and ^{58}Ni(α,n)^{61}Zn reactions at 67 and 19 MeV, respectively. Five lifetimes were measured for the first time, including the lifetime of the $5/2^-_1$ isomer at 124 keV. Short lifetimes from the RDDS analysis are corrected for Doppler-shift attenuation (DSA) in the target and stopper foils. Ambiguous observations in previous measurements were resolved. The obtained lifetimes are compared to predictions from different sets of shell-model calculations in the fp, $f_{5/2}pg_{9/2}$, and multishell fp-$g_{9/2}d_{5/2}$ model spaces. The band built on the $9/2^+_1$ state exhibits a prolate deformation with $\beta \approx 0.24$. Especially, the inclusion of cross-shell excitation into the $1d_{5/2}$ orbital is found to be decisive for the description of collectivity in the first excited positive-parity band.

DOI: 10.1103/PhysRevC.96.044313

I. INTRODUCTION

Nuclei in the $A \approx 60$–70 region, in the vicinity of ^{56}Ni, show a plethora of excitations, both single-particle and collective, associated with different prolate, oblate, and triaxial shapes. To cope with this variety, the theoretical description within the nuclear shell model has advanced substantially in recent years. The latest large-scale shell-model calculations surmount the limitations of previous truncation schemes in this mass region and employ successfully a multishell valence space. Moreover, the improved description of the effective nucleon-nucleon (NN) interaction is expected to create a consistent description of nuclei from the $N = Z$ line to the very exotic neutron-rich side of the Segrè chart. The neutron-deficient nucleus ^{61}Zn, which is subject to this study, is located within a transitional region midway between the $N = Z = 28$ shell closure and strongly deformed systems near ^{72}Kr [1,2]. With respect to the closure of the $0f_{7/2}$ shell, ^{61}Zn has two valence protons and three valence neutrons. In the valence spaces with doubly-magic ^{40}Ca as core, a total of 10 protons and 11 neutrons have to be considered.

The shell gap at $N = Z = 28$ separates the $|Nlj\rangle = 0f_{7/2}$ orbital from the $1p_{3/2}$, $0f_{5/2}$, and $1p_{1/2}$ shells within the so-called fp model space (cf. Fig. 1). The role of these orbitals is reflected by the presence of low-lying $1/2^-$, $3/2^-$, and $5/2^-$ states in nuclei throughout the mass $A \approx 60$ region. Natural-parity states with $\pi = +$ $(-)$ for even (odd) nuclei are generally well-described within the single-oscillator fp basis. However, particle excitations from the fp shell to the intruder high-j unique-parity $0g_{9/2}$ orbital play an important role for configurations of levels with only moderate excitation energies from intermediate to high spins in nuclei above ^{56}Ni.

Several shell-model interactions are available for the description of neutron-deficient $A \approx 60$ nuclei. Based on the inert core ^{40}Ca, well-established effective interactions such as GXPF1 [3], GXPF1A [4], KB3G [5], or FPD6 [6] include the $0f_{7/2}$, $1p_{3/2}$, $0f_{5/2}$, and $1p_{1/2}$ orbitals. The $N = Z = 28$ nucleus ^{56}Ni is considered doubly magic and serves as an inert core for shell-model calculations including the ($1p_{3/2}$, $0f_{5/2}$, $1p_{1/2}$) shell plus the positive-parity $\ell = 4$ $0g_{9/2}$ orbital below the $Z = N = 50$ shell closure (also referred to as the $f_{5/2}pg_{9/2}$ model space). However, the $0f_{7/2}$ orbital is neglected in this approach. Prominent interactions in this shell-model basis are jj44b [7] and JUN45 [8]. Both fp and $f_{5/2}pg_{9/2}$ calculations are limited in the sense that the $f_{7/2}$ and $g_{9/2}$ orbitals are not available simultaneously in the different model spaces. Thus, fp-shell calculations cannot describe negative-parity (positive-parity) bands and parity-changing transitions [9] in even (odd) nuclei. Early shell-model approaches discussed a sizable breaking of the $N = Z = 28$ magicity [10] and concluded ^{56}Ni to be a rather soft core. Indeed, in a full fp shell calculation employing the FPD6 Hamiltonian, Otsuka *et al.* [11] calculated the doubly-closed shell probability in the wave

*Corresponding author: andreas.vogt@ikp.uni-koeln.de

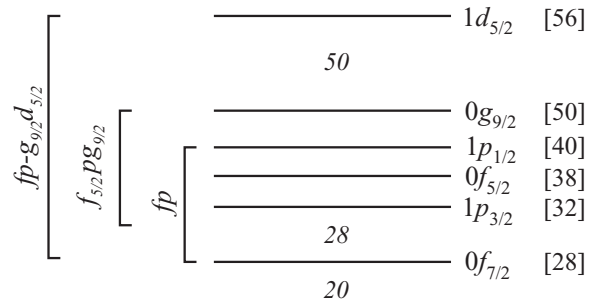

FIG. 1. Single-particle states above doubly-magic ^{40}Ca with shell closures at $N = Z = 20$, 28, and 50.

function of the ^{56}Ni ground state to be only 49%. Therefore, in the vicinity of ^{56}Ni multiparticle excitations from the $0f_{7/2}$ orbital play a non-negligible role for the construction of states ranging from low to high spins [12,13].

The most recent advances have been driven by the experimental accessibility of very neutron-rich systems above ^{56}Ni, for which the inclusion of the $\nu 0g_{9/2}$ orbital is indeed crucial to successfully describe energy spectra and transition strengths. Large-scale shell-model calculations in the multishell valence space comprising the fp shell plus the $\nu 0g_{9/2}$ and even $\nu 1d_{5/2}$ orbitals were both performed by the advanced Monte Carlo shell model (MCSM) [14] or by utilizing efficient massive parallelization of the Lanczos algorithm to solve the shell-model Hamiltonian for the largest matrix dimensions [15].

So far, several experimental studies have been carried out in ^{61}Zn. Firm spin and parity assignments of yrast and yrare excited states below 5 MeV were already performed in early studies, e.g., by populating ^{61}Zn in ^{58}Ni(α,n) [16–18], ^{58}Ni(^{6}Li,$p2n$), ^{54}Fe(^{10}B,$p2n$) [18], and ^{40}Ca(^{24}Mg,$2pn$) [18,19] fusion-evaporation reactions. Andersson *et al.* [20,21] investigated the level scheme of ^{61}Zn up to excitation energies of approximately 10 MeV employing the CLARION high-purity germanium (HPGe) detector array at the Oak Ridge National Laboratory coupled to the Recoil Mass Spectrometer (RMS) in the fusion-evaporation reaction ^{40}Ca(^{24}Mg,$2pn$) at 104 MeV. Furthermore, several superdeformed bands were discovered in ^{28}Si(^{36}Ar,$2pn$) and ^{40}Ca(^{29}Si,2α) experiments employing the GAMMASPHERE array at Lawrence Berkeley National Laboratory [22] and Argonne National Laboratory [22,23]. The CLARION experiment yielded a first estimate on the lifetime of the $5/2^-_1$ state 124 keV above the $3/2^-_{\text{g.s.}}$ ground state. The depopulating γ-ray intensity of the 124-keV transition did not match the total feeding intensity. Employing the simulation-based recoil-shadow technique, lifetime estimates of 10 and 6 ns were obtained for the hypothetical cases of pure dipole and quadrupole transitions, respectively. A lower lifetime limit of $\tau > 1$ ps was given by Schubank *et al.* [18] for various low-spin states in ^{61}Zn. A partial level scheme of ^{61}Zn, including transitions of interest to this paper, is presented in Fig. 2.

The present paper reports on two experiments performed at the FN-Tandem accelerator at the Institute for Nuclear Physics, University of Cologne to measure lifetimes of excited states in ^{61}Zn. A recoil-distance Doppler-shift (RDDS) experiment

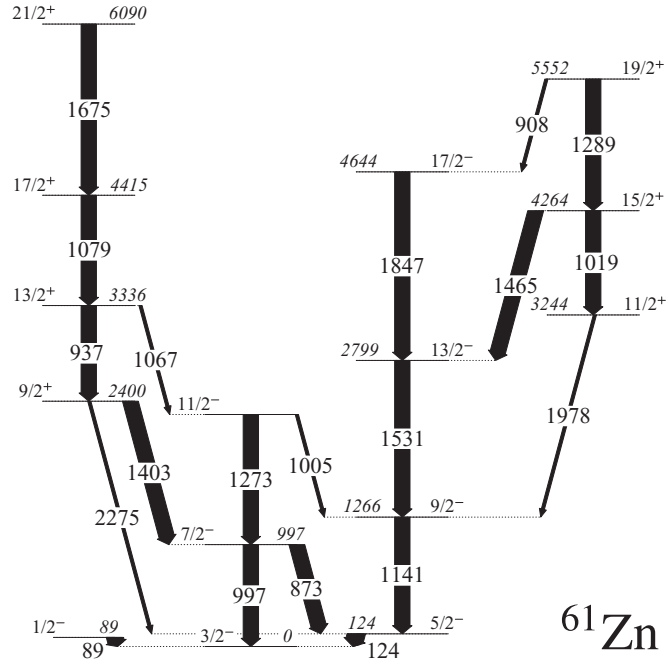

FIG. 2. Partial level scheme of ^{61}Zn including the first excited negative- and positive-parity bands. The reduced transition strengths of the 124-, 1141-, 1403-, 937-, and 1079-keV decays from the $5/2^-_1$, $9/2^-_1$, $9/2^+_1$, $13/2^+_1$, and $17/2^+_1$ states are the subject of this paper. Energies and spins are adopted from Ref. [20]. Dominating transitions are presented with thick arrows.

employing the Cologne coincidence plunger device was performed to measure lifetimes in the order of picoseconds. Lifetimes in the nanosecond region were addressed by utilizing electronic fast timing.

This paper is organized as follows: the experimental setup and data analysis of the two experiments are described in Sec. II. Experimental results and comparison with shell-model theory are presented in Secs. III and IV, respectively. The paper closes with a summary and conclusions in Sec. V.

II. EXPERIMENTAL DETAILS AND DATA ANALYSIS

A. Recoil-distance Doppler-shift experiment

The 10-MV FN-Tandem accelerator at the Institute of Nuclear Physics, University of Cologne provided a beam of ^{24}Mg with an energy of 77 MeV and an average beam current of 2 pnA in the RDDS experiment. The beam impinged onto a sandwich target consisting of 0.6(1)-mg/cm^2 99.9% enriched ^{40}Ca evaporated onto a gold backing of 2 mg/cm^2 thickness facing the beam. The back side was coated with a thin 0.05-mg/cm^2 gold layer in order to protect the ^{40}Ca layer from oxidation. The ^{61}Zn recoils left the target with a velocity of 2.5% of the speed of light and were stopped in a separate 7.3-mg/cm^2-thick tantalum foil. Utilizing the Cologne plunger device [24], target-to-stopper distances were chosen in the range from 41.7 to 140.6 μm. Beam-dependent changes such as thermal expansion of the target were compensated by an electronic feedback system employing a piezoelectric linear motor. The accuracy of the distances was measured to be better

than 0.7% in the relevant range of the target and stopper foils. An array of twelve high-purity germanium (HPGe) detectors was used to detect the emitted γ rays, placed in rings at 0° (1 detector), 45° (6 detectors), and 143° (5 detectors) with respect to the beam axis. To reduce background radiation arising from x rays, each detector was shielded by 2-mm-thick sheets of lead and copper. Data were collected at seven different target-to-stopper distances of 41.7, 45.6, 50.6, 55.6, 60.6, 70.6, and 140.6 μm and were sorted offline into two-dimensional $\gamma\gamma$ matrices corresponding to all possible ring-ring combinations for the different target-to-stopper distances. The lifetime analysis was performed by employing the differential decay-curve method (DDCM) [24–26] in coincidence mode. In this way, any uncertainties imposed by unknown side feeding were eliminated.

The recoil velocity v is needed for the DDC method; it is accurately determined via the observed Doppler shift of the in-flight components. Several statistically independent lifetimes are determined for the different target-to-stopper distances i, corresponding to certain flight times t_i, as well as from different ring-ring correlation groups. The final lifetime τ is calculated using the weighted mean of the different lifetimes τ_i, including only distances in the sensitive range as defined in Ref. [24]. Statistical uncertainties of the final lifetime values are dominated by the uncertainties of the single τ_i values. Scattering or slopes in the distribution of the single lifetime values τ_i plotted against the distances would indicate the presence of systematic errors. Remaining systematic uncertainties are mainly due to the distribution of the recoil velocities and can be adequately estimated.

In RDDS experiments, for lifetimes $\tau > 5$ ps the simplifying assumption is made that all nuclei decay either during flight in the vacuum and are detected Doppler-shifted, or decay while they are at rest in the stopper foil and, thus, are detected unshifted. The slowing-down processes in the target- and stopper foils are neglected. However, if the lifetime of the level of interest is comparable to the slowing down time of the recoiling nucleus, Doppler-shift attenuation can be observed between the shifted and unshifted peaks [27]. In order to correct for this effect, gated spectra are simulated with a Monte Carlo simulation taking into account the kinematics of the recoiling nuclei and the material properties of the target and stopper foils. These spectra are analyzed in the same way as the experimental spectra, without considering attenuation effects. Details on the simulation are given in Ref. [28]. Correction factors $c(\tau)$ as a function of the corresponding lifetime (see Fig. 3) are extracted from the comparison of the simulated lifetimes with the lifetimes analyzed from the simulated spectra. The impact of DSA on the lifetime is strongly depending on the recoil velocity. In previous publications, DSA was investigated to be relevant up to a lifetime of 3 ps at recoil velocities of <1% [28].

B. Electronic fast-timing experiment

Another experiment at the Cologne FN tandem accelerator focused on lifetimes in the nanosecond range. Excited states in the nucleus of interest were populated via the ^{58}Ni(α,n)^{61}Zn fusion-evaporation reaction at a beam energy of 19 MeV.

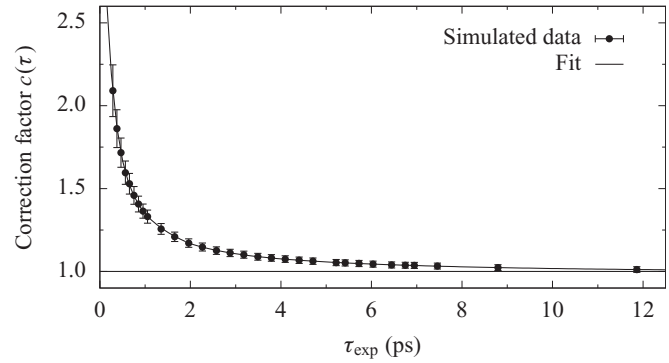

FIG. 3. Simulated Doppler-shift attenuation correction factor $c(\tau)$ as a function of the lifetime (data points). A line is drawn to guide the eye.

The recoils were stopped completely in the 2-mg/cm^2-thick, self-supporting >99.9%-enriched ^{58}Ni target. Lifetimes were measured with a fast-timing setup consisting of a mixed γ-ray detector array employing eight HPGe and eight cerium-doped lanthanum bromide ($LaBr_3$:Ce) detectors, mounted in the frame of the HORUS array [29]. Six of the $LaBr_3$:Ce detectors were surrounded by bismuth-germanate (BGO) veto detectors to suppress the Compton background [30]. The count rate of the individual detectors was maintained around 20 kHz. Furthermore, copper sheets were employed to reduce the x-ray background. Time differences between groups of $LaBr_3$:Ce detectors were measured by three time-to-amplitude converters (TAC) in a multiplexed-start and multiplexed-stop analog electronics circuit applying the method described in Refs. [31–33]. Detected energies and the TAC amplitudes were recorded in a triggerless mode using 80-MHz synchronized XIA^{TM} DGF-4C Rev. F digitizers and stored on disk. Information from the high-resolution HPGe detectors is crucial to judge the cleanliness of the reaction and to identify possible contaminations to the decays of interest. Double coincidences between two $LaBr_3$:Ce detectors and corresponding gated energy-time matrices were correlated offline using the sorting code SOCO-V2 [34,35]. By using a prompt γ-ray cascade of the ^{152}Eu calibration source, all $TAC_{i,j}$ spectra between every suitable detector-detector combination (i,j) were carefully aligned to a common offset t_0; in this way, different time delays within the setup were corrected. Final TAC_{ij} spectra were generated out of $(E_i; E_j; \Delta t_{ij})$ tuples which contain prompt, delayed, and antidelayed components. Each gating combination yields a delayed and antidelayed time distribution, as either the populating or the depopulating γ-ray can provide the start signal in the TAC. In general, the obtained time distributions are a convolution of the prompt response function (PRF), the time response of the setup, and the exponential decay. Lifetimes are extracted by fitting a function of the form $N(t) = a\exp(t/\tau) + b$ to the tail of the time distributions. The parameter b is determined from the background and kept constant.

Multipole mixing ratios of transitions between excited states $J_1 \xrightarrow{\delta_1} J_2 \xrightarrow{\delta_2} J_3$ are investigated with the $\gamma\gamma$ angular-correlation code CORLEONE [36,37] based on the phase

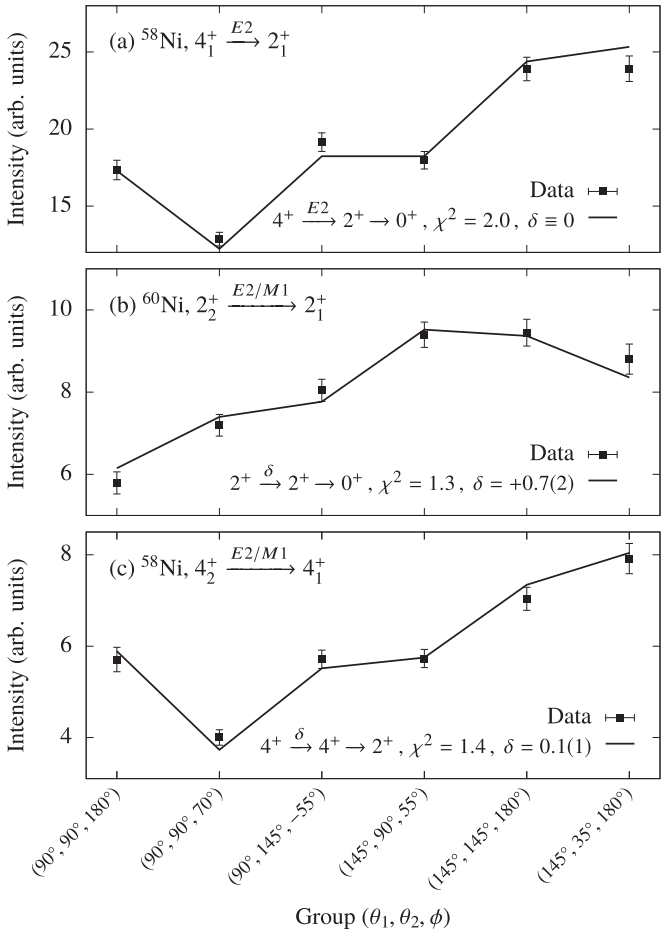

FIG. 4. $\gamma\gamma$ angular correlations fits. Experimental yields in the six correlation groups (θ_1,θ_2,ϕ) (data points) are compared to calculated angular-correlation functions $W(\theta_1,\theta_2,\phi)$ (lines) with the code CORLEONE. (a) Fit of the well-known $4_1^+ \xrightarrow{E2} 2_1^+ \xrightarrow{E2} 0_1^+$ 1004–1454-keV cascade in ^{58}Ni. The spin hypothesis shows good agreement with the experimental data. (b) Fit of the $2_2^+ \xrightarrow{\delta} 2_1^+ \xrightarrow{E2} 0_1^+$ cascade in ^{60}Ni. The evaluated multipole-mixing ratio is reproduced within its error. (c) Fit of the 1161–1004-keV $4_2^+ \xrightarrow{\delta} 4_1^+ \xrightarrow{E2} 2_1^+$ cascade in ^{58}Ni. See text for details.

convention by Krane, Steffen, and Wheeler [38,39]. The data of the ^{58}Ni$(\alpha,n)^{61}$Zn experiment were sorted into six correlation group matrices, each associated with detector pairs at angles $\theta_{1,2}$ with respect to the beam axis and a relative angle ϕ between the planes spanned by the detectors and the beam axis. Relative intensities in the correlation groups are then evaluated in χ^2 fits to angular correlation functions $W(\theta_1,\theta_2,\phi) \equiv W(J_1,J_2,J_3,\delta_1,\delta_2)$. A fit to the well-known $4_1^+ \to 2_1^+ \to 0_1^+$ electric-quadrupole cascade in ^{60}Ni is used to renormalize the initial efficiency-corrected intensities of the angular-correlation groups. The anisotropy corrections are subsequently applied to fits of other cascades. Details on the CORLEONE analysis are given in Refs. [40,41].

Figure 4 shows the comparison of the theoretical angular-correlation functions (lines) with relative intensities obtained from the experimental correlation groups (data points). A benchmark fit of the $4_1^+ \to 2_1^+$ 1004-keV transition in ^{58}Ni in Fig. 4(a) yields a good agreement with the expected $E2$ character. Similarly, the evaluated multipole-mixing ratio $\delta_{\text{lit.}} = +0.93(2)$ of the $2_2^+ \to 2_1^+$ decay in ^{60}Ni [42] is well reproduced [$\delta_{\text{expt.}} = +0.7(2)$] within its uncertainty in Fig. 4(b). In the same way, the large uncertainty of the evaluated $4_2^+ \to 4_1^+$ mixing ratio in ^{58}Ni ($\delta_{\text{lit.}} = +0.6^{+3}_{-6}$) [43] can be narrowed down to $\delta_{\text{expt.}} = +0.1(1)$.

III. RESULTS

A. $9/2^-$ state at 1266 keV

The lifetime of the first excited $9/2^-$ state at 1266 keV is accessible via the RDDS experiment. The level decays by a 1141-keV transition to the $5/2_1^-$ state. In the DDC analysis, a gate was set on the Doppler-shifted component of the directly feeding 1531-keV $13/2_1^- \to 9/2_1^-$ transition. Gated γ-ray spectra in Figs. 5(d_1) to 5(d_7), exemplarily projected from a $\gamma\gamma$-coincidence matrix of all detectors against the detectors in forward direction, demonstrate the evolution of the peak intensities in the Doppler-shifted and unshifted components with increasing flight distance of the ^{61}Zn recoils. Deduced lifetimes for each target-to-stopper distance and the corresponding weighted mean (black solid line) together with its 1σ deviation (black dashed lines) are shown in Fig. 5(a). Exemplary intensity distributions of the shifted in-flight components of the $9/2_1^- \to 5/2_1^-$ transition are presented as black points in Fig. 5(b), the ones of the stopped unshifted components in Fig. 5(c). The fitted second-order polynomials are printed in red lines. The two largest distances are excluded in the final lifetime analysis as they are outside of the sensitive range. Intensity distributions in forward and backward rings are analyzed independently; the deduced lifetimes are 0.99(15) and 1.06(18) ps, respectively. Their weighted mean is 1.02(11) ps, the DSA-corrected final value is $1.37 \pm 0.14(\text{stat.})\,^{+0.08}_{-0.06}(\text{syst.})$ ps.

B. $9/2^+$ state at 2400 keV

The $9/2_1^+$ state at 2400 keV is long-lived compared to the previously discussed $9/2_1^-$ state. According to the description in Sec. III A, fitted lifetime curves are presented in Figs. 5(e) to 5(g). Gates on feeding transitions yield only small intensities of the Doppler-shifted in-flight peaks. However, a narrow gate from below, applied on the full unshifted (stopped) peak of the depopulating transition, can be employed for the lifetime analysis [24]. Lifetimes are determined by analyzing both Doppler-shifted and total intensities of the feeding $13/2_1^+ \to 9/2_1^+$ transition. Corresponding gated spectra are shown in Figs. 5(h_1) to 5(h_7). A drawback of this technique is posed by feeding-related effects in which the original nuclear spin alignment diminishes in flight due to hyperfine interactions with the electron shells, also called deorientation [44]. Impact from deorientation is examined with a gate set on the 1403-keV transition covering both in-flight and stopped peaks. The full intensity of the feeding transition at 937 keV is determined for every distance. As a result, no systematic change of the sum intensity to larger target-to-stopper distances and longer flight times is observed, thus, there is no significant deorientation. The lifetimes calculated for data from forward

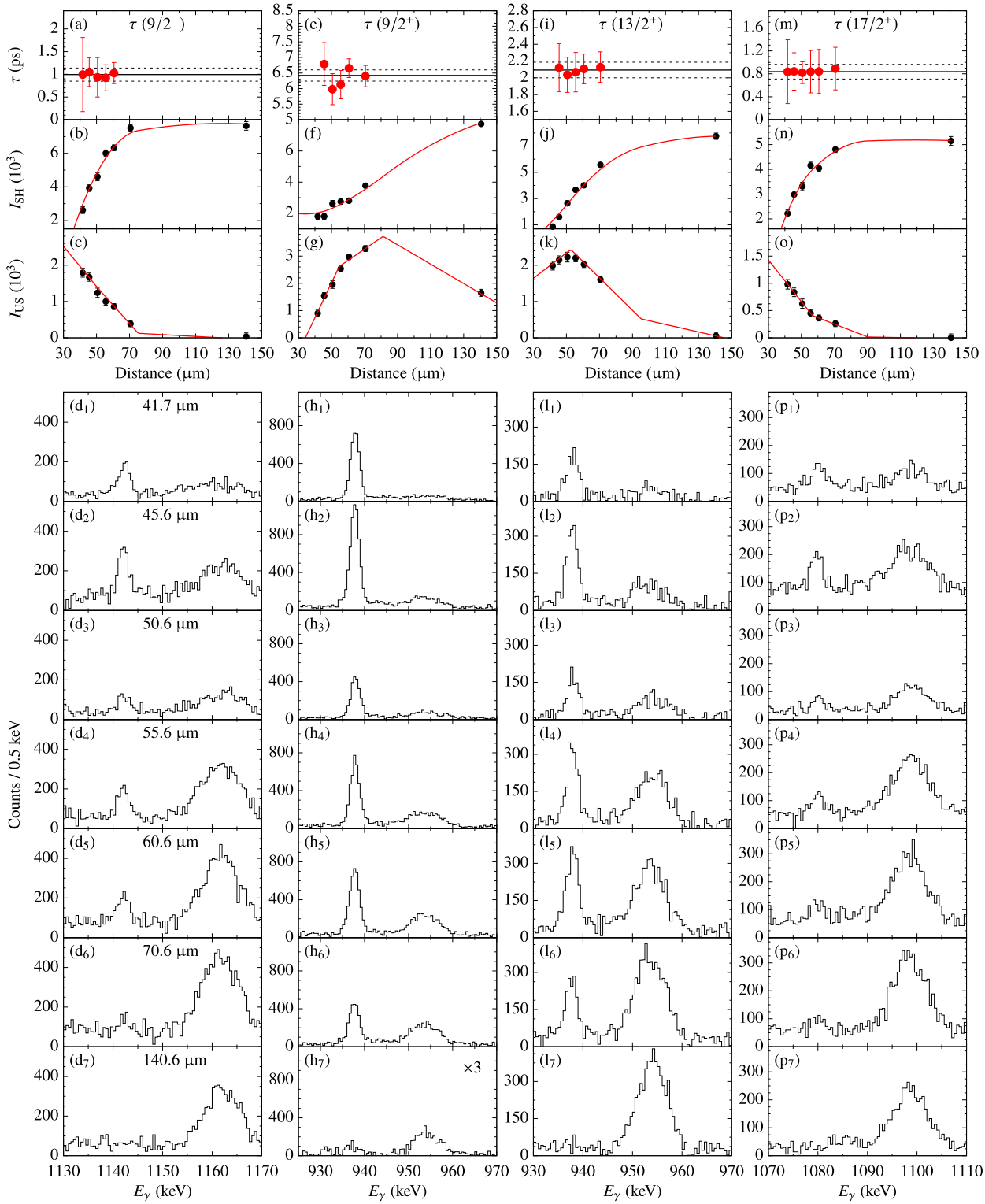

FIG. 5. Extracted lifetimes (top row), intensity distributions of Doppler-shifted (second row) and unshifted peaks (third row), gated spectra of detectors at about 45° for the different target-to-stopper distances, generated by a gate on the shifted peak of the feeding transition for the (a,b,c,d_{1-7}) $9/2^-_1 \rightarrow 5/2^-_1$, (i,j,k,$l_{1-7}$) $13/2^+_1 \rightarrow 9/2^+_1$, and (m,n,o,$p_{1-7}$) $17/2^+_1 \rightarrow 13/2^+_1$ transitions. The lifetime of the $9/2^+_1$ state is deduced from γ-ray spectra of the feeding $13/2^+_1 \rightarrow 9/2^+_1$ transitions (e,f,g,h_{1-7}), generated by a gate on the deexciting 1403-keV γ rays. See text for details.

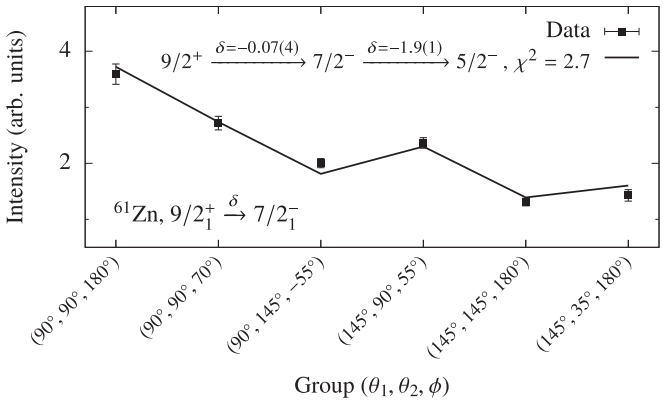

FIG. 6. $\gamma\gamma$ angular correlations fits of the 1403–873-keV $9/2_1^+ \xrightarrow{\delta} 7/2_1^- \xrightarrow{E2/M1} 5/2_1^-$ cascade in ^{61}Zn. The nomenclature is similar to that of Fig. 4.

[$\tau = 6.42(18)$ ps] and backward rings [$\tau = 6.25(18)$ ps] agree within the error bars. When using a gate from below, the lifetime is less affected by DSA, as coincidences of two γ rays subsequently emitted during the slowing-down process do not contribute to the analyzed lifetime. Thus, the lifetime of the $13/2_1^+$ state is not corrected. Possible DSA effects are included in the systematic error; the final weighted mean lifetime is $6.34 \pm 0.13(\text{stat.})\ ^{+0.41}_{-0.32}(\text{syst.})$ ps.

Detailed knowledge of the $M2/E1$ multipole-mixing ratio δ is required to deduce $B(E1)$ and $B(M2)$ transition strengths for the $9/2_1^+ \rightarrow 7/2_1^-$ transition. The corresponding angular-correlation fit for the $9/2_1^+ \rightarrow 7/2_1^-$ transition, shown in Fig. 6, gives a dominating $E1$ character with a measured mixing ratio of $\delta = -0.07(4)$. The experimental intensities are obtained by a gate on the depopulating 873-keV $7/2_1^- \rightarrow 5/2_1^-$ $E2/M1$ transition of which the $E2/M1$ mixing ratio is known to be $\delta = -1.9(1)$ [45].

C. $13/2^+$ state at 3336 keV

The DDCM analysis of the 937-keV $13/2_1^+ \rightarrow 9/2_1^+$ transition is again performed by exploiting gates on the feeding 1079-keV $17/2_1^+ \rightarrow 13/2_1^+$ transition. Gated spectra are shown in Figs. 5(l_1) to 5(l_7). The fit analysis [cf. Figs. 5(j) and 5(k)] yields $\tau = 2.09(9)$ ps for forward and $\tau = 2.13(11)$ ps for the backward direction with a weighted mean of $\tau = 2.11(7)$ ps. After DSA corrections a lifetime of $\tau = 2.44 \pm 0.08(\text{stat.}) \pm 0.10(\text{syst.})$ ps is obtained.

D. $17/2^+$ state at 4415 keV

The lifetime of the $17/2_1^+$ state at 4415 keV was determined by gating on the Doppler-shifted component of the directly feeding 1675-keV $21/2_1^+ \rightarrow 17/2_1^+$ transition. Owing to a contamination caused by two coincident γ-ray transitions in ^{61}Cu with $E_\gamma = 1642.2$ keV and 1065.6 keV [45] under backward angles, lifetimes for the $17/2_1^+$ state were only determined from intensity distributions in the forward detectors. Three second-order polynomials are fitted to the intensity distributions of seven distances in Figs. 5(n) and 5(o). Six distances were included in the calculation of the lifetime. Although the three distances between 55.6 and 70.6 μm are per definition not inside the sensitive range, they were taken into account for the lifetime calculation yielding $\tau = 0.84(13)$ ps. The difference between the weighted mean lifetimes obtained with and without these additional data points is small compared to the systematic and statistical errors. The final DSA-corrected lifetime of the $17/2_1^+$ state is determined to be $\tau = 1.19 \pm 0.18(\text{stat.})\ ^{+0.06}_{-0.04}(\text{syst.})$ ps.

E. $5/2^-$ state at 124 keV

The study of the $5/2_1^- \rightarrow 3/2^-_{\text{g.s.}}$ ground-state decay was subject to the electronic fast-timing experiment. Singles γ-ray spectra of both $LaBr_3$:Ce and HPGe detectors are presented in Fig. 7(a). Relevant transitions of the negative-parity bands feeding the $5/2_1^-$ state are marked with vertical dashed lines. Major contaminations stem from the main (α, $xnyp$) reaction channels ^{61}Cu, ^{58}Ni, and ^{60,61}Ni. While the $7/2_1^- \rightarrow 5/2_1^-$ and $9/2_1^- \rightarrow 5/2_1^-$ feeding transitions can be resolved in the HPGe spectrum but not in the $LaBr_3$:Ce spectrum, the $5/2_1^- \rightarrow 3/2_1^-$ ground-state transition is well separated from other peaks and, thus, can also be resolved by the scintillation detectors. Therefore, coincidences between each two $LaBr_3$:Ce detectors are sufficient to clean the spectra from contaminating peaks in order to investigate the decay curve of the 124-keV transition. A corresponding $\gamma\gamma$ projection gated on 124 keV is shown in Fig. 7(b). $\gamma\gamma$ delayed-coincidence time spectra were generated by correlating the directly feeding $9/2_1^- \rightarrow 5/2_1^-$ and $7/2_1^- \rightarrow 5/2_1^-$ transitions as well as the indirectly feeding $13/2_1^- \rightarrow 9/2_1^-$ transitions with the $5/2_1^- \rightarrow 3/2^-_{\text{g.s.}}$ transition. The indirect gate is applicable since the lifetime of the $9/2_1^-$ state is considered prompt as it is by three orders of magnitude shorter (cf. Sec. III A) than the lifetime of the state of interest. As the $5/2_1^-$ state has a lifetime in the nanosecond range, a fit is applied to the exponential slope of the delayed time distribution. Antidelayed time spectra are inverted around the position of the prompt peak and subsequently added to the corresponding delayed spectra as described in Ref. [46]. The summed time spectra are presented in Fig. 7 for the aforementioned 124–1141-keV (c), 124–873-keV (d), and 124–1531-keV (e) gate combinations. The short-lived component is mainly caused by Compton background. Exponential fits of the long-lived slope component yield lifetimes of 4.66(3), 4.63(3), and 4.63(5) ns, respectively. Constant background is included in the fit model. The independently determined lifetimes utilizing the three different gate conditions show excellent agreement. Systematic errors from background contributions at the borders of the fit interval as well as uncertainties in the determination of the background parameter are conservatively taken into account for the final weighted mean lifetime value of 4.6(1) ns.

The multipole-mixing ratio of the 124-keV $5/2_1^- \rightarrow 3/2^-_{\text{g.s.}}$ transition is necessary to calculate corresponding $M1$ and $E2$ transition strengths. Various values were published: To date, the most precise value of $\delta = -0.05(2)$ was measured by Schubank *et al.* [18]. Smith *et al.* [16] constrained the mixing ratio to either $\delta = -0.01^{+11}_{-7}$ or -3.2^{+11}_{-17}. In the most recent work by Andersson *et al.* a mixing of $\delta(E2/M1) \approx 1$ was

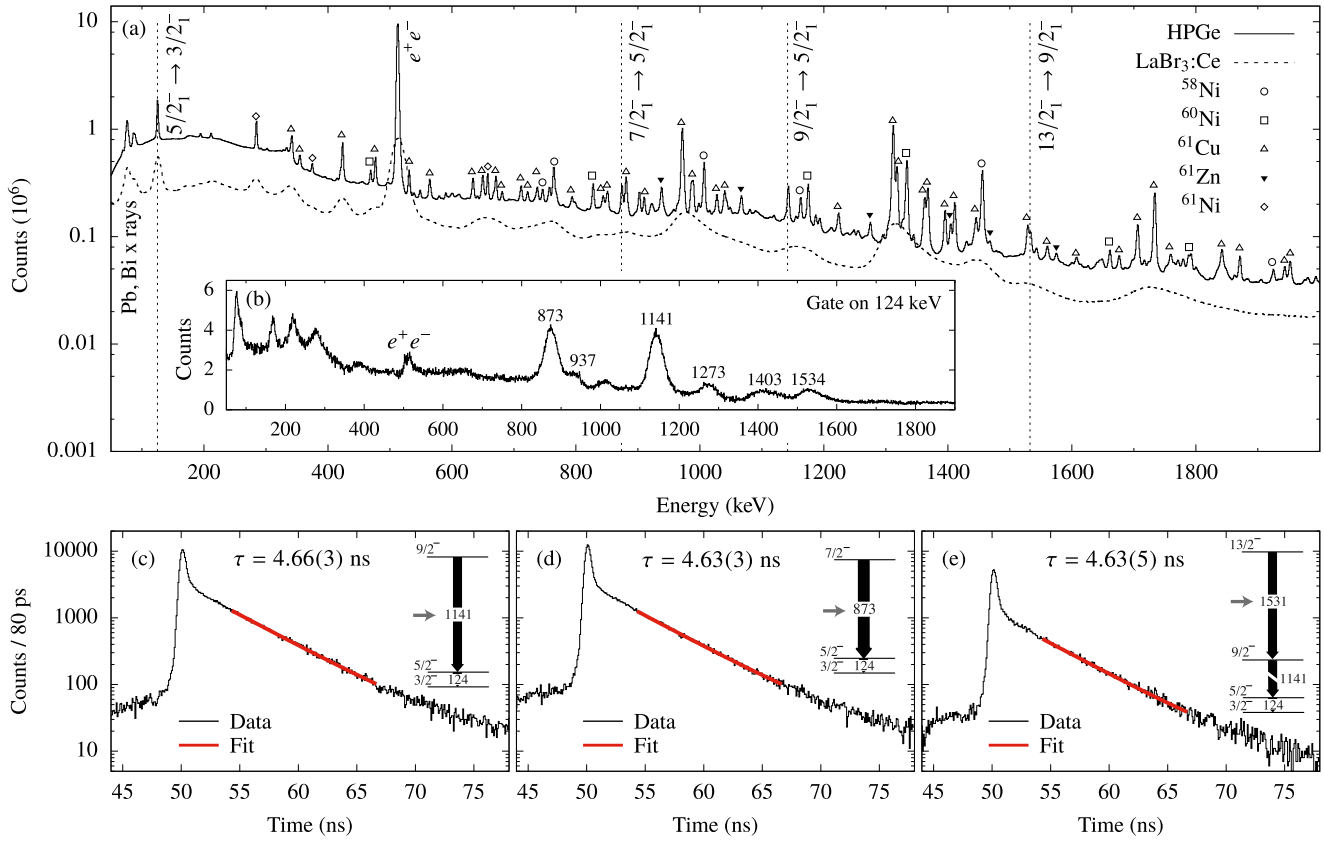

FIG. 7. Top: (a) Comparison of $LaBr_3$:Ce and HPGe γ-ray spectra from the ^{58}Ni$(\alpha,n)^{61}$Zn fast-timing experiment. Note the limited energy resolution of the $LaBr_3$:Ce scintillators. The $5/2_1^- \to 3/2_1^-$ transition at 124 keV is well resolved and separated from neighboring peaks in both spectra. Peaks from the other reaction and decay products ^{58,60,61}Ni [42,43] and ^{61}Cu [45] are labeled. Solid triangles mark γ-ray transitions of ^{61}Zn. (b) $LaBr_3$:Ce $\gamma\gamma$ projection with a gate on 124 keV in $LaBr_3$:Ce. Bottom: Gated $\gamma\gamma$-delayed time distributions and final lifetime fits for the gating combinations (c) 1141 keV $9/2_1^- \to 5/2_1^-$ and 124 keV $5/2_1^- \to 3/2_1^-$, (d) 873 keV $7/2_1^- \to 5/2_1^-$ and 124 keV $5/2_1^- \to 3/2_1^-$, (e) 1531 keV $13/2_1^- \to 9/2_1^-$ and 124 keV $5/2_1^- \to 3/2_1^-$. Lifetimes are determined by exponential fits of the delayed component. The fit is drawn with a red solid line. Random background is determined separately and incorporated into the fit.

extrapolated from recoil-shadow simulations [20]. Figure 8 shows a $\gamma\gamma$ angular-correlation fit similar to the one shown in Sec. III B. Experimental intensities of the 1141-keV transition are obtained by a gate on 124 keV. The fit model only considers the mixing of the depopulating 124-keV transition as the pure $E2$ multipole character of the 1141-keV is well established. Two indistinguishable χ^2 minima are found, leading to either $\delta = -0.007(33)$ (solid line) or $\delta = -3.7^{+4}_{-6}$ (dashed line). The $\delta = 1$ hypothesis (dotted line) can be clearly rejected.

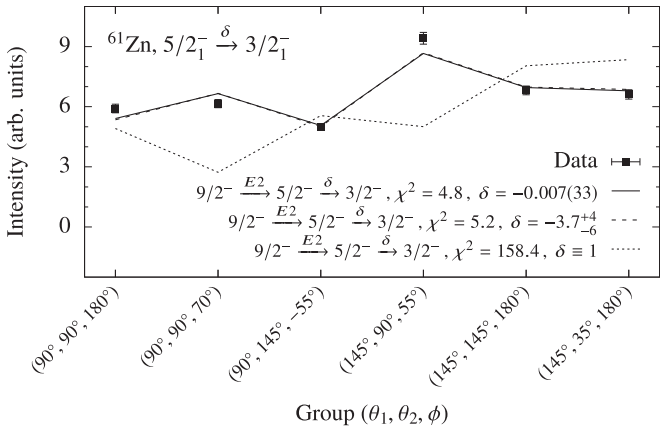

FIG. 8. $\gamma\gamma$ angular-correlation fits to the 1141–124-keV cascade. Based on the known $E2$ character of the $9/2_1^- \to 5/2_1^-$ transition, two minima are found for the 124-keV transition, giving either $\delta = -0.007(33)$ (solid line) or $\delta = -3.7^{+4}_{-6}$ (dashed line). The dotted line corresponds to a $\delta = 1$ hypothesis.

IV. SHELL-MODEL CALCULATIONS

The experimentally obtained lifetimes and corresponding reduced transition probabilities in ^{61}Zn are compared to shell-model theory. Shell-model calculations were carried out employing the shell-model code NUSHELLX@MSU [47] as well as the massive-parallelization code KSHELL [48]. Figure 9 shows the comparison of experimental and theoretical energy spectra. Reduced transition probabilities obtained within this work are summarized in Tables I and II.

The first calculation was performed in the $f_{5/2}pg_{9/2}$ valence space outside of the core ^{56}Ni. With only five valence particles, no truncation is necessary. The jj44b Hamiltonian by Brown *et al.* [7] yields an overall good agreement with the experimental first excited states, especially for the

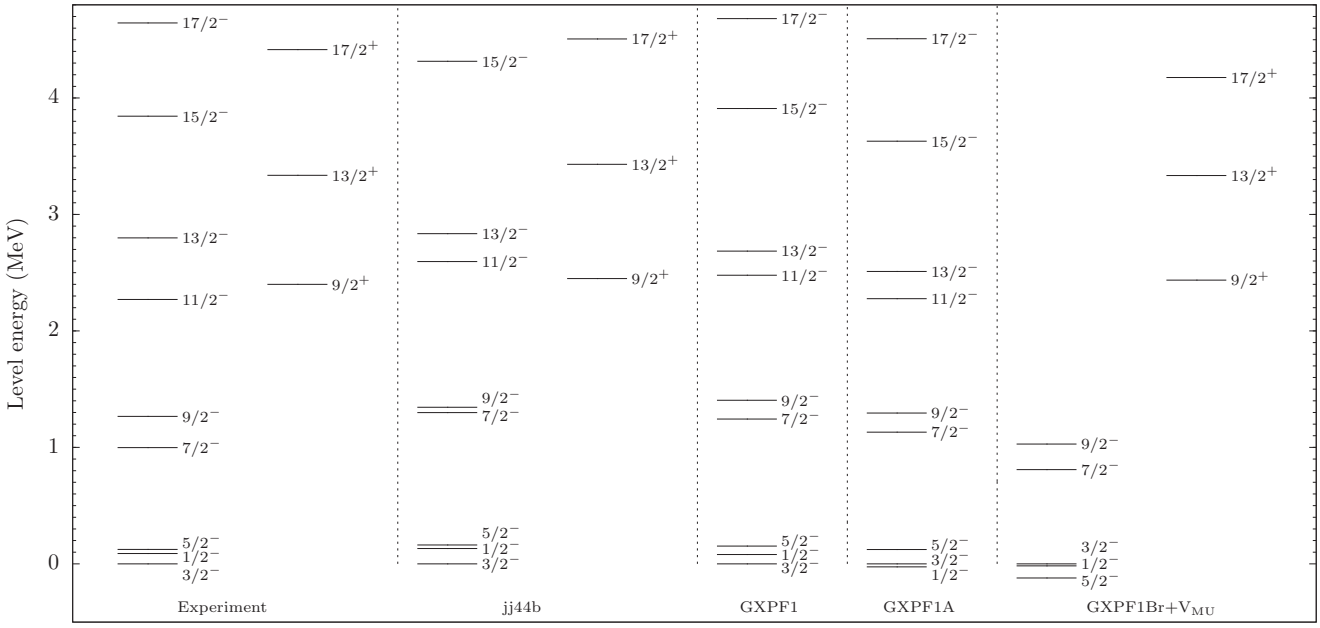

FIG. 9. Comparison between experimental and theoretical level energies for ^{61}Zn using various SM interactions. Negative- and positive-parity states are separated into different columns for better visibility. See text for details on the SM calculations.

positive-parity band. The low-spin levels are reproduced in the correct order. Nonetheless, the quadrupole transition strengths within the $17/2^+_1 \rightarrow 13/2^+_1 \rightarrow 9/2^+_1$ band and of the $9/2^-_1 \rightarrow 5/2^-_1$ transition are severely underestimated.

Further calculations were carried out employing the GXPF1 [3] and GXPF1A [4] interactions which include $0f_{7/2}$-orbit excitations across the shell boundary at $Z,N = 28$, but do not include the $0g_{9/2}$ subshell. To cope for computational limitations, a truncation is introduced which permits excitations of three protons and neutrons each from the $0f_{7/2}$ orbital to nonrestricted higher-lying orbits. Excitation energies of the negative-parity states are generally well reproduced; however, the GXPF1A interaction interchanges the first excited states and predicts the $1/2^+_1$ state 26 keV below the $3/2^-_1$ ground state. A precise reproduction of the 124-keV $5/2^-_1 \rightarrow 3/2^-_1$ transition is achieved by the GXPF1A interaction with $E_{\gamma,\mathrm{calc.}} = 123$ keV. While GXPF1 yields a good agreement within <115 keV for states with $J \geqslant 13\hbar$, the GXPF1A interaction systematically underpredicts the excitation energies of these states. For the comparison of reduced transition strengths, two different sets of effective charges are chosen: (i) $e_\pi = 1.5e$ and $e_\nu = 0.5e$ as proposed by Honma *et al.* [50] and (ii) $e_\pi = 1.15e$ and $e_\nu = 0.8e$ as deduced by du Rietz *et al.* [49] from their study of ^{51}Fe and ^{51}Mn. The fp-shell interactions provide a fair agreement with the experimental $B(E2; 9/2^-_1 \rightarrow 5/2^-_1)$ transition strength employing effective charges of $e_\pi = 1.5e$ and $e_\nu = 0.5e$ (cf. Table I), however slightly underestimating the collectivity. This is also reflected in the splitting, i.e., level spacing, of the $11/2^-$ and $13/2^-$ levels which is predicted too small by the fp-shell calculations. The $5/2^-_1 \rightarrow 3/2^-_1$ transition is strongly quenched, which makes the corresponding $B(M1)$ and $B(E2)$ transition strengths rather sensitive to the total wave functions of the states involved in the transition. The theoretical $B(M1)$ transition strength of the $5/2^-_1 \rightarrow 3/2^-_1$ transition is calculated to be 0.0035 W.u. using the GXPF1 interaction and

TABLE I. Experimental reduced quadrupole transition strengths of the $17/2^+_1 \rightarrow 13/2^+_1$, $13/2^+_1 \rightarrow 9/2^+_1$, and $9/2^-_1 \rightarrow 5/2^-_1$ transitions. Final lifetimes of the corresponding excited states are corrected for DSA. The transition strengths are compared to shell-model calculations employing the jj44b, GXPF1, GXPF1A, and GXPF1Br+V_{MU} interactions. Two different sets of effective charges, (A) $e_\pi = 1.5e$, $e_\nu = 0.5e$ and (B) $e_\pi = 1.15e$, $e_\nu = 0.8e$ [49], are employed. See text for details.

$J^\pi_i \rightarrow J^\pi_f$	E_i (keV)	τ_i (ps) ±(stat.) ±(syst.)	$B(E2)\downarrow$ (e^2fm^4) Expt.	Theory jj44b	GXPF1		GXPF1A		GXPF1Br +V_{MU}	
				$(e_{\pi,\nu})_A$	$(e_{\pi,\nu})_A$	$(e_{\pi,\nu})_B$	$(e_{\pi,\nu})_A$	$(e_{\pi,\nu})_B$	$(e_{\pi,\nu})_A$	$(e_{\pi,\nu})_B$
$\frac{9}{2}^- \rightarrow \frac{5}{2}^-$	1266	$1.37 \pm 0.14^{+0.08}_{-0.06}$	309^{+38}_{-32}	205	254	242	257	243	253	239
$\frac{13}{2}^+ \rightarrow \frac{9}{2}^+$	3336	$2.44 \pm 0.08 \pm 0.10$	465^{+26}_{-23}	224					332	331
$\frac{17}{2}^+ \rightarrow \frac{13}{2}^+$	4415	$1.19 \pm 0.18^{+0.06}_{-0.04}$	471^{+86}_{-64}	210					314	314

TABLE II. Experimental reduced transition strengths and multipole-mixing ratios of the mixed-multipolarity $9/2_1^+ \rightarrow 7/2_1^-$ and $5/2_1^- \rightarrow 3/2_1^-$ transitions. Calculated transition strengths are given individually for the corresponding $E1$, $M1$, $E2$, and $M2$ character in Weisskopf units. Effective charges are chosen as $e_\pi = 1.5e$ and $e_\nu = 0.5e$. Multipole-mixing ratios follow the convention of Krane, Steffen, and Wheeler [38,39].

$J_i^\pi \rightarrow J_f^\pi$	E_i (keV)	τ_i (ps) $\pm$(stat.) $\pm$(syst.)	$\sigma\lambda$	δ	$B(\sigma\lambda)\downarrow$ (W.u.)				
					Expt.	Theory			
						jj44b	GXPF1	GXPF1A	GXPF1Br $+V_{\mathrm{MU}}$
$\frac{9}{2}^+ \rightarrow \frac{7}{2}^-$	2400	$6.34 \pm 0.13^{+0.41}_{-0.32}$	$E1$	$-0.07(4)$	0.00035^{+3}_{-2}	[a]			<0.0001
			$M2$		0.4^{+6}_{-3}	0.33			0.15
$\frac{5}{2}^- \rightarrow \frac{3}{2}^-$	124	$4.6(1) \times 10^3$	$M1$	$-0.05(2)$	0.0035^{+8}_{-8}	<0.0001	0.0035	0.0026	0.0042
			$E2$		1.0^{+10}_{-6}	1.47	0.09	0.20	0.13

[a] $E1$ strengths cannot be evaluated in the $f_{5/2}pg_{9/2}$ model space.

free-nucleon g factors—an excellent agreement with the experimental value of $B(M1; 5/2_1^- \rightarrow 3/2_1^-) = 0.0035(8)$ W.u. A similar theoretical result for the $M1$ strength was already reported by Ekman *et al.* with a GXPF1 calculation employing a much tighter truncation, allowing for a total of three isospin-independent holes in the $0f_{7/2}$ shell and up to five particle excitations out of the proton and neutron $1p_{3/2}$ orbits [51]. In contrast, the GXPF1A interactions falls short in reproducing the $B(M1)$ strength of the $5/2_1^- \rightarrow 3/2_1^-$ transition within the experimental error. The theoretical multipole-mixing ratio is calculated to be $\delta = 0.02$ (GXPF1) and $\delta = 0.03$ (GXPF1A), respectively. This result is in good agreement with the values from $\gamma\gamma$ correlations obtained in this work as well with the previous values by Smith *et al.* [16] ($\delta = 0.01^{+0.11}_{-0.07}$) and Schubank *et al.* [18] ($\delta = 0.05(2)$).

In a third approach, a multishell valence space is adopted. The calculation is carried out in the $(0f_{7/2}, 1p_{3/2}, 0f_{5/2}, 1p_{1/2})$ shell, enlarged by the $0g_{9/2}$ and $1d_{5/2}$ orbits. Calculations within this large valence space allow us to describe both negative- and positive-parity states of ^{61}Zn. The Hamiltonian is composed of two parts: (i) for the fp-shell orbits the GXPF1Br [52] effective interaction, a modification of the GXPF1A interaction to reproduce neutron-rich $^{51-54}$Ca isotopes; and (ii) for the cross-shell NN interaction between the fp-shell and the gds-shell orbits the monopole-based universal force (V_{MU}) [53], refined by adding the M3Y spin-orbit force [54]. The V_{MU} interaction consists of the central force and the $\pi + \rho$ meson-exchange tensor force. The mass-dependent scaling of the two-body matrix elements is $(A/42)^{-0.3}$. Spurious center-of-mass motion due to the excitation beyond major shells is encountered with the introduction of the parameter $\beta_{\mathrm{c.m.}}\hbar\omega/A \approx 10$ MeV as proposed by Gloeckner and Lawson [55]. The Hamiltonian matrix is diagonalized within the m scheme by the Lanczos method employing the code KSHELL [48]. Further details can be found in Ref. [15]. A truncation is introduced so that the $0f_{7/2}$ configuration is limited to six holes, and one proton or neutron is allowed to occupy the $0g_{9/2}$ or $1d_{5/2}$ orbits. The maximum of this m-scheme dimension is $d = 9.9 \times 10^9$.

The GXPF1Br+V_{MU} calculation yields a reasonable agreement with the experimental transition strengths along the positive-parity band. Although the theoretical $B(E2)$ values underpredict the experimental results, the agreement is superior with respect to the jj44b interaction. However, the low-lying $3/2_1^-$, $1/2_1^-$, and $5/2_1^-$ states are predicted in a reversed order. Both sets of effective charges, i.e., ($e_\pi = 1.5e$, $e_\nu = 0.5e$) and ($e_\pi = 1.15e$, $e_\nu = 0.8e$), give comparable transition strengths. Average occupation numbers in each involved single-particle orbit are presented in Table III. The configurations of the positive-parity states on top of the $9/2_1^+$ state are mainly driven by the excitation of one neutron to the $0g_{9/2}$ orbital. Interestingly, the $1d_{5/2}$ orbit has a perturbative but decisive role for the description of these states. The impact of the inclusion of the $1d_{5/2}$ orbital in the GXPF1Br+V_{MU} calculation on level energies and quadrupole transition strengths in ^{61}Zn is shown in Table IV. By including the $1d_{5/2}$ orbital, the experimental energies of both the $9/2_1^+$ and $13/2_1^+$ states are reproduced within 36 and 2 keV, respectively. In contrast, the calculation with the truncation that one proton or neutron is only allowed to occupy the $0g_{9/2}$ orbit, i.e., prohibiting excitations into the $1d_{5/2}$ orbital, fails to reproduce the experimental energies by 527 and 588 keV. Including the $1d_{5/2}$ orbital, the excitation energy of the $17/2_1^+$ state is underpredicted by 239 keV, otherwise it is overpredicted by 178 keV. Theoretical $B(E2; 17/2_1^+ \rightarrow 13/2_1^+)$ and $B(E2; 13/2_1^+ \rightarrow 9/2_1^+)$ transition strengths are computed to be 314 and 332 $e^2\mathrm{fm}^4$, respectively. Consequently, the $1d_{5/2}$ orbital is as important as the $0g_{9/2}$ orbital to describe the $E2$ collectivity in the first excited positive-parity band.

A significant collectivity enhancement is generated by the $1d_{5/2}$ orbital, although its neutron orbital occupancy is only

TABLE III. Average occupation numbers in each single-particle orbit of the $(0f_{7/2}, 1p_{3/2}, 0f_{5/2}, 1p_{1/2}, 0g_{9/2}, 1d_{5/2})$ valence space along the positive-parity band, calculated with the GXPF1Br+V_{MU} interaction.

J^π		$0f_{7/2}$	$1p_{3/2}$	$0f_{5/2}$	$1p_{1/2}$	$0g_{9/2}$	$1d_{5/2}$
$9/2_1^+$	π	7.276	1.263	1.025	0.378	0.052	0.006
	ν	7.435	1.421	0.850	0.352	0.860	0.082
$13/2_1^+$	π	7.311	1.192	0.990	0.444	0.057	0.006
	ν	7.464	1.367	0.807	0.424	0.840	0.097
$17/2_1^+$	π	7.222	1.149	1.232	0.326	0.065	0.006
	ν	7.386	1.330	1.040	0.314	0.862	0.067

TABLE IV. Level energies and quadrupole transition strengths from the GXPF1Br+$V_{\rm MU}$ calculations including ("w/") and neglecting ("w/o") excitations into the $1d_{5/2}$ orbital. Similarly, excitations from the $0f_{7/2}$ orbital are either allowed up to six holes ($0f_{7/2}$ active) or forbidden in a fully occupied truncation ($0f_{7/2}$ inactive). Effective charges are chosen as $e_\pi = 1.5e$ and $e_\nu = 0.5e$.

J_i^π	E_i (MeV)			$B(E2; J_i \to J_i - 2)$ (e^2fm^4)				
	Expt.	w/o $1d_{5/2}$	w/ $1d_{5/2}$	Expt.	$0f_{7/2}$ inactive w/o $1d_{5/2}$	$0f_{7/2}$ inactive w/ $1d_{5/2}$	$0f_{7/2}$ active w/o $1d_{5/2}$	$0f_{7/2}$ active w/ $1d_{5/2}$
$9/2_1^+$	2.400	2.957	2.436					
$13/2_1^+$	3.336	3.924	3.334	465^{+26}_{-23}	187	220	252	332
$17/2_1^+$	4.415	4.593	4.176	471^{+86}_{-64}	171	200	220	314

0.082 for the $9/2_1^+$ state and 0.097 for the $13/2_1^+$ state. This point is investigated further by comparing the employed truncation of the $0f_{7/2}$ orbital, allowing for up to six holes ($0f_{7/2}$ active), with a fully occupied truncation ($0f_{7/2}$ inactive). Corresponding $B(E2)$ values of the $17/2_1^+ \to 13/2_1^+$ and $13/2_1^+ \to 9/2_1^+$ transitions are calculated by (i) allowing (w/ $1d_{5/2}$) and (ii) prohibiting (w/o $1d_{5/2}$) an excitation into the $1d_{5/2}$ orbital, respectively (cf. Table IV). If no excitation is allowed into the $1d_{5/2}$ orbital, the collectivity enhancement of the $0f_{7/2}$ orbital, which is not included in jj44b interaction, is around 30%. On the other hand, in the case of an allowed $1d_{5/2}$ excitation, the enhancement effect of the particle-hole excitation from the $0f_{7/2}$ orbital is more than 50%. This indicates that both the $0f_{7/2}$ and $1d_{5/2}$ orbits coherently contribute to the increased quadrupole collectivity. Apart from that, the inclusion of the $1d_{5/2}$ orbital does not affect results for the negative-parity states. The calculation of a two-particle excitation into the $0g_{9/2}$ orbital is not feasible as the m-scheme dimension would exceed the computational limit of $d = 10^{10}$. However, examining the calculations in the $f_{5/2}pg_{9/2}$ valence space, a significant contribution from pair excitations is expected only starting at $J^\pi = 21/2_1^-$ in first excited negative-parity states and at $J^\pi = 27/2_1^+$ in the corresponding positive-parity states.

Total potential energy surfaces (PES) are constructed employing a Q-constrained Hartree-Fock calculation with variation after parity projection. Details on the calculation of PES are given in Ref. [15]. Results are shown in Fig. 10(a) for negative-parity states and in Fig. 10(b) for positive-parity states. Both PES indicate a prolate shape of ^{61}Zn. However, the positive-parity states are more deformed than the negative-parity ones, confirming the deformation-driving role of the $0g_{9/2}$ orbital [1]. Theoretical intrinsic quadrupole moments are extracted from calculated $B(E2; I \to I - 2)$ values using the expression [56]

$$B(E2; I_i K \to I_f K) = \frac{5}{16\pi} e^2 Q_0^2 |\langle I2K0|I-2\,K\rangle|^2, \quad (1)$$

with $\langle I2\,K0|I-2\,K\rangle$ being the Clebsch-Gordon coefficient of a transition from spin (I,K) to $(I-2,K)$ considering pure $E2$ multipolarity. A body-fixed system is introduced by assuming K quantum numbers, $K = 1/2$ and $K = 9/2$, which correspond to the decoupling limit and the strong coupling limit, respectively.

Figure 10(c) shows the calculated Q_0 values for the band members built on the $9/2_1^+$ state for $K = 1/2$ (red squares) and for $K = 9/2$ (blue diamonds); both experimental values $eQ_0(13/2_1^+; K = 1/2) = 121^{+4}_{-3}$ $e$fm^2 and $eQ_0(17/2_1^+; K = 1/2) = 119^{+11}_{-8}$ $e$fm^2 are drawn as black points assuming $K = 1/2$. Whereas the quadrupole moments for $K = 1/2$ are roughly constant, the intrinsic quadrupole moment of the $13/2_1^+$ state is much larger than for the other states in the strong coupling limit of $K = 9/2$. This behavior indicates that the picture of the decoupling limit is favorable. Quadrupole deformations β relate to Q_0 via

$$\beta = \frac{\sqrt{5\pi}}{3} \frac{1}{Z R_0^2} Q_0, \quad (2)$$

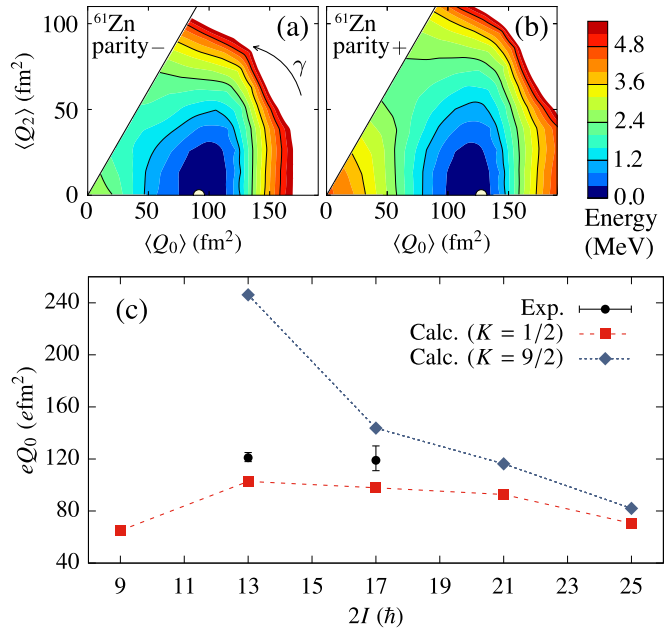

FIG. 10. Total energy surfaces for the (a) negative (natural) and (b) positive (unnatural) parity states in ^{61}Zn. Energy minima are indicated with white circles. (c) Electric intrinsic quadrupole moments for members of the band built on the $9/2_1^+$ state in ^{61}Zn. Spins I on the horizontal axis are denoted as $2I$. Experimental values (black circles) are calculated assuming $K = 1/2$. Calculated quadrupole moments with $K = 1/2$ (red squares) and $K = 9/2$ (blue diamonds) correspond to the decoupling limit and the strong coupling limit, respectively.

with $R_0 = 1.2\,A^{1/3}$ fm. Constant values of $\beta_{13/2^+} = 0.24(4)$ and $\beta_{17/2^+} = 0.24(7)$ are obtained along the positive-parity band.

V. CONCLUSIONS

Lifetimes in ^{61}Zn were investigated by means of the recoil-distance Doppler-shift (RDDS) and the electronic fast-timing methods. The first excited $5/2^-_1$ state is confirmed to be isomeric with a half-life of 4.6(1) ns. Transition strengths of four other transitions were measured for the first time, including two transitions in the first-excited positive-parity band: the parity-changing $9/2^+_1 \rightarrow 7/2^-_1$ transition and the $9/2^-_1 \rightarrow 5/2^-_1$ transition. Simulated correction factors of Doppler-shift attenuation effects in the target and stopper foils of the RDDS setup are applied to the experimental results.

Based on the inert core ^{40}Ca, the well-established GXPF1 and GXPF1A interactions reproduce energies and lifetimes of the low-lying negative-parity states. However, fp-shell calculations cannot describe positive-parity bands and parity-changing transitions. Calculations in the $f_{5/2}pg_{9/2}$ valence space do not reproduce the experimental transition strength due to an expected sizable breaking of the $N = Z = 28$ magicity. A new multi-shell approach within the fp-$g_{9/2}d_{5/2}$ space employing an effective Hamiltonian composed of the GXPF1Br interaction for fp-shell orbits and the universal interaction V_{MU} for the $0g_{9/2}$ and $1d_{5/2}$ orbits reproduces the properties of the positive-parity band reasonably. Collective properties of the positive-parity band cannot be explained by neglecting the $1d_{5/2}$ orbital. A parity-projected Q-constrained Hartree-Fock calculation indicates a prolate deformation of ^{61}Zn; positive-parity states are more deformed than the negative-parity ones.

The level scheme of the $T_z = +1/2$ mirror partner ^{61}Ga was investigated by Andersson *et al.* [57] employing recoil-$\gamma\gamma$ coincidences. In contrast to ^{61}Zn, no evidence for a positive-parity band was found in the more exotic ^{61}Ga. The γ-ray decay of such states may be disfavored and an explanation for the nonobservation of a positive-parity band was given by a possible proton-decay branch from the $g_{9/2}$ orbital. Detailed knowledge of ^{61}Zn will aid the improvement of theoretical predictions and, therefore, be beneficial for future experiments in ^{61}Ga.

Further experimental studies of neighboring nuclei along the $T_z = -1/2$ isodiasphere are desirable. In both ^{59}Cu and ^{63}Ga only lower limits or estimates are available for the half-lives of the low-lying $5/2^-_1$ states, $T_{1/2} > 1.1$ ps [58] and $T_{1/2} \approx 25$ ns [59], respectively. Despite some known transition strengths of parity-changing transitions depopulating $9/2^+_1$ states, for example in ^{65}Ge [60], only scarce information is available on lifetimes of higher-lying positive-parity states. Future experiments focusing on lifetimes in this region will help us to understand the evolution of the $0g_{9/2}$ orbital and its interplay with the $1d_{5/2}$ orbital for the construction of positive-parity high-spin states in this region.

ACKNOWLEDGMENTS

We thank the IKP FN Tandem accelerator team for the professional support during the experiment. T.T. and N.S. acknowledge the support by "Priority Issue on post-K computer" (Elucidation of the Fundamental Laws and Evolution of the Universe, hp170230) and the HPCI system research project (hp170182). A.V. and L.K. acknowledge support from the Bonn-Cologne Graduate School of Physics and Astronomy (BCGS).

[1] A. Gade, D. Bazin, A. Becerril, C. M. Campbell, J. M. Cook, D. J. Dean, D.-C. Dinca, T. Glasmacher, G. W. Hitt, M. E. Howard, W. F. Mueller, H. Olliver, J. R. Terry, and K. Yoneda, Quadrupole Deformation of the Self-Conjugate Nucleus ^{72}Kr, Phys. Rev. Lett. **95**, 022502 (2005).

[2] E. Nácher, A. Algora, B. Rubio, J. L. Taín, D. Cano-Ott, S. Courtin, Ph. Dessagne, F. Maréchal, Ch. Miehé, E. Poirier, M. J. G. Borge, D. Escrig, A. Jungclaus, P. Sarriguren, O. Tengblad, W. Gelletly, L. M. Fraile, and G. Le Scornet, Deformation of the $N = Z$ Nucleus ^{76}Sr Using β-Decay Studies, Phys. Rev. Lett. **92**, 232501 (2004).

[3] M. Honma, T. Otsuka, B. A. Brown, and T. Mizusaki, Effective interaction for pf-shell nuclei, Phys. Rev. C **65**, 061301 (2002).

[4] M. Honma, T. Otsuka, B. A. Brown, and T. Mizusaki, Shell-model description of neutron-rich pf-shell nuclei with a new effective interaction GXPF 1, Eur. Phys. J. A **25**, 499 (2005).

[5] A. Poves, J. Sánchez-Solano, E. Caurier, and F. Nowacki, Shell model study of the isobaric chains $A = 50$, $A = 51$ and $A = 52$, Nucl. Phys. A **694**, 157 (2001).

[6] W. A. Richter, M. G. Van Der Merwe, R. E. Julies, and B. A. Brown, New effective interactions for the $0f1p$ shell, Nucl. Phys. A **523**, 325 (1991).

[7] B. Cheal, E. Mané, J. Billowes, M. L. Bissell, K. Blaum, B. A. Brown, F. C. Charlwood, K. T. Flanagan, D. H. Forest, C. Geppert, M. Honma, A. Jokinen, M. Kowalska, A. Krieger, J. Krämer, I. D. Moore, R. Neugart, G. Neyens, W. Nörtershäuser, M. Schug, H. H. Stroke, P. Vingerhoets, D. T. Yordanov, and M. Žáková, Nuclear Spins and Moments of Ga Isotopes Reveal Sudden Structural Changes between $N = 40$ and $N = 50$, Phys. Rev. Lett. **104**, 252502 (2010), and references within.

[8] M. Honma, T. Otsuka, T. Mizusaki, and M. Hjorth-Jensen, New effective interaction for f_5pg_9-shell nuclei, Phys. Rev. C **80**, 064323 (2009).

[9] O. Izotova, D. Rudolph, J. Ekman, C. Fahlander, A. Algora, C. Andreoiu, R. Cardona, C. Chandler, G. de Angelis, E. Farnea, A. Gadea, J. Garcés Narro, J. Nyberg, M. Palacz, Zs. Podolyák, T. Steinhardt, and O. Thelen, Survey of $E1$ transitions in the mass $A \sim 60$ region, Phys. Rev. C **69**, 037303 (2004).

[10] S. S. M. Wong and W. G. Davies, A shell model study of the structure of ^{56}Ni, Phys. Lett. B **28**, 77 (1968).

[11] T. Otsuka, M. Honma, and T. Mizusaki, Structure of the $N = Z = 28$ Closed Shell Studied by Monte Carlo Shell Model Calculation, Phys. Rev. Lett. **81**, 1588 (1998).

[12] A. F. Lisetskiy, N. Pietralla, M. Honma, A. Schmidt, I. Schneider, A. Gade, P. von Brentano, T. Otsuka, T. Mizusaki,

and B. A. Brown, Experimental evidence for ^{56}Ni-core breaking from the low-spin structure of the $N = Z$ nucleus $^{58}_{29}Cu_{29}$, Phys. Rev. C **68**, 034316 (2003).

[13] K. Minamisono, P. F. Mantica, T. J. Mertzimekis, A. D. Davies, M. Hass, J. Pereira, J. S. Pinter, W. F. Rogers, J. B. Stoker, B. E. Tomlin, and R. R. Weerasiri, Nuclear Magnetic Moment of the ^{57}Cu Ground State, Phys. Rev. Lett. **96**, 102501 (2006).

[14] Y. Tsunoda, T. Otsuka, N. Shimizu, M. Honma, and Y. Utsuno, Novel shape evolution in exotic Ni isotopes and configuration-dependent shell structure, Phys. Rev. C **89**, 031301 (2014).

[15] T. Togashi, N. Shimizu, Y. Utsuno, T. Otsuka, and M. Honma, Large-scale shell-model calculations for unnatural-parity high-spin states in neutron-rich Cr and Fe isotopes, Phys. Rev. C **91**, 024320 (2015).

[16] P. J. Smith, L. P. Ekstrom, F. Kearns, P. J. Twin, and N. J. Ward, Gamma-ray spectroscopy of ^{61}Zn and a planar germanium polarimeter system, J. Phys. G **8**, 281 (1982).

[17] J. M. Thirion, G. Chouraqui, Th. Muller, and M. Port, Gamma-ray spectroscopy of ^{61}Zn, Z. Phys. A **317**, 329 (1984).

[18] R. B. Schubank, J. A. Cameron, and V. P. Janzen, Gamma-ray spectroscopy of ^{60,61}Zn and ^{59,60}Cu, Phys. Rev. C **40**, 2310 (1989).

[19] S. M. Vincent, P. H. Regan, S. Mohammadi, D. Blumenthal, M. Carpenter, C. N. Davids, W. Gelletly, S. S. Ghugre, D. J. Henderson, R. V. F. Janssens, M. Hjorth-Jensen, B. Kharraja, C. J. Lister, C. J. Pearson, D. Seweryniak, J. Schwartz, J. Simpson, and D. D. Warner, Near yrast study of the fpg shell nuclei ^{58}Ni, ^{61}Cu, and ^{61}Zn, Phys. Rev. C **60**, 064308 (1999).

[20] L-L. Andersson, D. Rudolph, J. Ekman, C. Fahlander, E. K. Johansson, R. du Rietz, C. J. Gross, P. A. Hausladen, D. C. Radford, and G. Hammond, γ-ray spectroscopy of excited states in $^{61}_{30}Zn_{31}$, Eur. Phys. J. A **30**, 381 (2006).

[21] L.-L. Andersson, The Mirror Nuclei ^{61}Ga and ^{61}Zn, Licentiate thesis, Lund University, 2006 (unpublished).

[22] C.-H. Yu, C. Baktash, J. Dobaczewski, J. A. Cameron, C. Chitu, M. Devlin, J. Eberth, A. Galindo-Uribarri, D. S. Haslip, D. R. LaFosse, T. J. Lampman, I.-Y. Lee, F. Lerma, A. O. Macchiavelli, S. D. Paul, D. C. Radford, D. Rudolph, D. G. Sarantites, C. E. Svensson, J. C. Waddington, and J. N. Wilson, Comparison of superdeformed bands in ^{61}Zn and ^{60}Zn: Possible evidence for $T = 0$ pairing, Phys. Rev. C **60**, 031305 (1999).

[23] L.-L. Andersson, I. Ragnarsson, D. Rudolph, E. K. Johansson, D. A. Torres, C. Andreoiu, M. P. Carpenter, R. J. Charity, C. J. Chiara, J. Ekman, C. Fahlander, C. Hoel, O. L. Pechenaya, W. Reviol, R. du Rietz, D. G. Sarantites, D. Seweryniak, L. G. Sobotka, and S. Zhu, Comprehensive γ-ray spectroscopy of rotational bands in the $N = Z + 1$ nucleus ^{61}Zn, Phys. Rev. C **79**, 024312 (2009).

[24] A. Dewald, O. Möller, and P. Petkov, Developing the Recoil Distance Doppler-Shift technique towards a versatile tool for lifetime measurements of excited nuclear states, Prog. Part. Nucl. Phys. **67**, 786 (2012).

[25] A. Dewald, S. Harissopulos, and P. von Brentano, The differential plunger and the differential decay curve method for the analysis of recoil distance Doppler-shift data, Z. Phys. A **334**, 163 (1989).

[26] G. Böhm, A. Dewald, P. Petkov, and P. von Brentano, The differential decay curve method for the analysis of Doppler shift timing experiments, Nucl. Instrum. Methods Phys. Res., Sect. A **329**, 248 (1993).

[27] K. A. Gladnishki, P. Petkov, A. Dewald, C. Fransen, M. Hackstein, J. Jolie, Th. Pissulla, W. Rother, and K. O. Zell, Yrast electromagnetic transition strengths and shape coexistence in ^{182}Pt, Nucl. Phys. A **877**, 19 (2012).

[28] B. Saha, A. Dewald, O. Möller, R. Peusquens, K. Jessen, A. Fitzler, T. Klug, D. Tonev, P. von Brentano, J. Jolie, B. J. P. Gall, and P. Petkov, Probing nuclear structure of ^{124}Xe, Phys. Rev. C **70**, 034313 (2004).

[29] L. Netterdon, V. Derya, J. Endres, C. Fransen, A. Hennig, J. Mayer, C. Müller-Gatermann, A. Sauerwein, P. Scholz, M. Spieker, and A. Zilges, The γ-ray spectrometer HORUS and its applications for nuclear astrophysics, Nucl. Instrum. Methods Phys. Res., Sect. A **754**, 94 (2014).

[30] J.-M. Régis, M. Dannhoff, J. Jolie, C. Müller-Gatermann, and N. Saed-Samii, On the time response of background obtained in γ-ray spectroscopy experiments using $LaBr_3$(Ce) detectors with different shielding, Nucl. Instrum. Methods Phys. Res., Sect. A **811**, 42 (2016).

[31] J.-M. Régis, G. Pascovici, J. Jolie, and M. Rudigier, The mirror symmetric centroid difference method for picosecond lifetime measurements via coincidences using very fast $LaBr_3$(Ce) scintillator detectors, Nucl. Instrum. Methods Phys. Res., Sect. A **622**, 83 (2010).

[32] J.-M. Régis, H. Mach, G. S. Simpson, J. Jolie, G. Pascovici, N. Saed-Samii, N. Warr, A. Bruce, J. Degenkolb, L. M. Fraile, C. Fransen, D. G. Ghita, S. Kisyov, U. Koester, A. Korgul, S. Lalkovski, N. Mărginean, P. Mutti, B. Olaizola, Z. Podolyak, P. H. Regan, O. J. Roberts, M. Rudigier, L. Stroe, W. Urban, and D. Wilmsen, The generalized centroid difference method for picosecond sensitive determination of lifetimes of nuclear excited states using large fast-timing arrays, Nucl. Instrum. Methods Phys. Res., Sect. A **726**, 191 (2013).

[33] J.-M. Régis, N. Saed-Samii, M. Rudigier, S. Ansari, M. Dannhoff, A. Esmaylzadeh, C. Fransen, R.-B. Gerst, J. Jolie, V. Karayonchev, C. Müller-Gatermann, and S. Stegemann, Reduced γ-γ time walk to below 50 ps using the multiplexed-start and multiplexed-stop fast-timing technique with $LaBr_3$(Ce) detectors, Nucl. Instrum. Methods Phys. Res., Sect. A **823**, 72 (2016).

[34] N. Saed-Samii, Lifetime measurements using the FATIMA array in combination with EXOGAM@ILL, Diploma thesis, Universität zu Köln, 2013 (unpublished).

[35] N. Saed-Samii, computer code SOCO-V2, 2017 https://gitlab.ikp.uni-koeln.de/nima/soco-v2.

[36] I. Wiedenhöver, computer code CORLEONE, 1997.

[37] I. Wiedenhöver, O. Vogel, H. Klein, A. Dewald, P. von Brentano, J. Gableske, R. Krücken, N. Nicolay, A. Gelberg, P. Petkov, A. Gizon, J. Gizon, D. Bazzaco, C. Rossi Alvarez, G. de Angelis, S. Lunardi, P. Pavan, D. R. Napoli, S. Frauendorf, F. Dönau, R. V. F. Janssens, and M. P. Carpenter, Detailed angular correlation analysis with 4π spectrometers: Spin determinations and multipolarity mixing measurements in ^{128}Ba, Phys. Rev. C **58**, 721 (1998).

[38] K. S. Krane and R. M. Steffen, Determination of the $E2/M1$ Multipole Mixing Ratios of the Gamma Transitions in ^{110}Cd, Phys. Rev. C **2**, 724 (1970).

[39] K. S. Krane, R. M. Steffen, and R. M. Wheeler, Directional correlations of gamma radiations emitted from nuclear states oriented by nuclear reactions or cryogenic methods, At. Data Nucl. Data Tables **11**, 351 (1973).

[40] B. Fu, M. Seidlitz, A. Blazhev, M. Bouhelal, F. Haas, P. Reiter, K. Arnswald, B. Birkenbach, C. Fransen, G. Friessner, A. Hennig, H. Hess, R. Hirsch, L. Lewandowski, D. Schneiders, B. Siebeck, T. Steinbach, T. Thomas, A. Vogt, A. Wendt, K. Wolf, and K. O. Zell, γ-ray spectroscopy of ^{33}P and ^{33}S after fusion-evaporation reactions, Phys. Rev. C **94**, 034318 (2016).

[41] A. Linnemann, Das HORUS-Würfelspektrometer und Multi-phononanregungen in ^{106}Cd, Ph.D. thesis, Universität zu Köln, 2006.

[42] E. Browne and J. K. Tuli, Nuclear Data Sheets for $A = 60$, Nucl. Data Sheets **114**, 1849 (2013).

[43] D. D. Nesaraja, S. D. Geraedts, and B. Singh, Nuclear Data Sheets for $A = 58$, Nucl. Data Sheets **111**, 897 (2010).

[44] P. Petkov, A. Dewald, A. Gelberg, G. Böhm, P. Sala, P. von Brentano, and W. Andrejtscheff, The nuclear deorientation effect in ^{122}Xe and ^{128}Ba, Nucl. Phys. A **589**, 341 (1995).

[45] K. Zuber and B. Singh, Nuclear Data Sheets for $A = 61$, Nucl. Data Sheets **125**, 1 (2015).

[46] V. Karayonchev, J.-M. Régis, J. Jolie, A. Blazhev, R. Altenkirch, S. Ansari, M. Dannhoff, F. Diel, A. Esmaylzadeh, C. Fransen, R.-B. Gerst, K. Moschner, C. Müller-Gatermann, N. Saed-Samii, S. Stegemann, N. Warr, and K. O. Zell, Evolution of collectivity in the $N = 100$ isotones near ^{170}Yb, Phys. Rev. C **95**, 034316 (2017).

[47] B. A. Brown and W. D. M. Rae, The Shell-Model Code NuShellX@MSU, Nucl. Data Sheets **120**, 115 (2014).

[48] N. Shimizu, Nuclear shell-model code for massive parallel computation, "KSHELL", arXiv:1310.5431.

[49] R. du Rietz, J. Ekman, D. Rudolph, C. Fahlander, A. Dewald, O. Möller, B. Saha, M. Axiotis, M. A. Bentley, C. Chandler, G. de Angelis, F. Della Vedova, A. Gadea, G. Hammond, S. M. Lenzi, N. Mărginean, D. R. Napoli, M. Nespolo, C. Rusu, and D. Tonev, Effective Charges in the fp Shell, Phys. Rev. Lett. **93**, 222501 (2004).

[50] M. Honma, T. Otsuka, B. A. Brown, and T. Mizusaki, New effective interaction for pf-shell nuclei and its implications for the stability of the $N = Z = 28$ closed core, Phys. Rev. C **69**, 034335 (2004).

[51] J. Ekman, C. Fahlander, and D. Rudolph, Mirror symmetry in the upper fp shell, Mod. Phys. Lett. A **20**, 2977 (2005).

[52] D. Steppenbeck, S. Takeuchi, N. Aoi, P. Doornenbal, M. Matsushita, H. Wang, H. Baba, N. Fukuda, S. Go, M. Honma, J. Lee, K. Matsui, S. Michimasa, T. Motobayashi, D. Nishimura, T. Otsuka, H. Sakurai, Y. Shiga, P.-A. Söderström, T. Sumikama, H. Suzuki, R. Taniuchi, Y. Utsuno, J. J. Valiente-Dobón, and K. Yoneda, Evidence for a new nuclear "magic number" from the level structure of ^{54}Ca, Nature (London) **502**, 207 (2013).

[53] T. Otsuka, T. Suzuki, M. Honma, Y. Utsuno, N. Tsunoda, K. Tsukiyama, and M. Hjorth-Jensen, Novel Features of Nuclear Forces and Shell Evolution in Exotic Nuclei, Phys. Rev. Lett. **104**, 012501 (2010).

[54] G. Bertsch, J. Borysowicz, H. McManus, and W. G. Love, Interactions for inelastic scattering derived from realistic potentials, Nucl. Phys. A **284**, 399 (1977).

[55] D. H. Gloeckner and R. D. Lawson, Spurious center-of-mass motion, Phys. Lett. B **53**, 313 (1974).

[56] A. Bohr and B. R. Mottelson, *Nuclear Structure, Volume II: Nuclear Deformations* (World Scientific, Singapore, 1998).

[57] L-L. Andersson, E. K. Johansson, J. Ekman, D. Rudolph, R. du Rietz, C. Fahlander, C. J. Gross, P. A. Hausladen, D. C. Radford, and G. Hammond, Identification of excited states in $^{61}_{31}$Ga$_{30}$: Mirror nuclei in the upper fp shell, Phys. Rev. C **71**, 011303 (2005).

[58] C. M. Baglin, Nuclear Data Sheets for $A = 59$, Nucl. Data Sheets **95**, 215 (2002).

[59] B. Erjun and H. Junde, Nuclear Data Sheets for $A = 63$, Nucl. Data Sheets **92**, 147 (2001).

[60] J. Görres, T. Chapuran, D. P. Balamuth, and J. W. Arrison, Structure of the Very Neutron-Deficient Ge Region: ^{64}Ge and ^{65}Ge, Phys. Rev. Lett. **58**, 662 (1987).